optica

Experimental investigation of silicon and silicon nitride platforms for phase-change photonic in-memory computing

Xuan Li,[1] Nathan Youngblood,[1] Zengguang Cheng,[1] Santiago Garcia-Cuevas Carrillo,[2] Emanuele Gemo,[2] Wolfram H. P. Pernice,[3] C. David Wright,[2] and Harish Bhaskaran[1,*]

[1]Department of Materials, University of Oxford, Oxford, UK
[2]Department of Engineering, University of Exeter, UK
[3]Department of Physics, University of Münster, Germany
*Corresponding author: harish.bhaskaran@materials.ox.ac.uk

Received 27 September 2019; revised 20 January 2020; accepted 21 January 2020 (Doc. ID 379228); published 3 March 2020

Advances in artificial intelligence have greatly increased demand for data-intensive computing. Integrated photonics is a promising approach to meet this demand in big-data processing due to its potential for wide bandwidth, high speed, low latency, and low-energy computing. Photonic computing using phase-change materials combines the benefits of integrated photonics and co-located data storage, which of late has evolved rapidly as an emerging area of interest. In spite of rapid advances of demonstrations in this field on both silicon and silicon nitride platforms, a clear pathway towards choosing between the two has been lacking. In this paper, we systematically evaluate and compare computation performance of phase-change photonics on a silicon platform and a silicon nitride platform. Our experimental results show that while silicon platforms are superior to silicon nitride in terms of potential for integration, modulation speed, and device footprint, they require trade-offs in terms of energy efficiency. We then successfully demonstrate single-pulse modulation using phase-change optical memory on silicon photonic waveguides and demonstrate efficient programming, memory retention, and readout of > 4 bits of data per cell. Our approach paves the way for in-memory computing on the silicon photonic platform.

https://doi.org/10.1364/OPTICA.379228

1. INTRODUCTION

Demands for applying silicon (Si) photonics to high-performance computing systems have grown significantly in recent years due to the breakdown of Dennard scaling [1] and information transfer bottlenecks in the conventional von Neumann architecture [2,3]. Data processing on photonic platforms is a promising approach because of the potential advantages over electrical approaches, where large bandwidth, high efficiency, ultrafast modulation speed, and low cross talk are crucial [4]. Critical photonic components, such as lasers [5], modulators [6], switches [7], filters [8], multiplexers [9,10], photodetectors [11–15], and memory cells, have been developed on different material platforms, such as silicon nitride (SiN), GeSi, III-V semiconductors, and others [16–18], with silicon-on-insulator (SOI) being the dominant platform. Furthermore, Si waveguides, owing to their thermal conductivity performance, have the potential to be doped to act as integrated heaters to enable wider applications [19]. As a consequence, compatibility with other on-chip photonic components, fabless and large-scale Si photonic integrated circuits (PICs) and other multiple features offer a promising route to future commercialization for Si platforms.

To date, Si PIC's ability to modulate, address, and retrieve data has mainly been based on thermo-optic effects and free-carrier dispersion effects. This commonly requires continuous biasing and high power consumption [20–22]. Integrating phase-change materials with integrated photonics offers nonvolatility for all-optical data addressing and retrieval. This has been demonstrated using a phase-change alloy, $Ge_2Sb_2Te_5$ (GST) coupled evanescently to photonic waveguides [4,23]. Since then, much progress has been made, such as both volatile and nonvolatile storage over 5 bits per cell [24,25], electrical and optical mixed-mode devices [26–28], reconfigurable optical cavities [29,30], logical operations [31,32], and optical switches [33–37]. Phase-change optical memory (PCOM) photonics has also been applied to photonic computing and artificial neural networks, such as implementation of accumulative addition [38], multiplication [39], optical synapses [40], and most recently, deep-learning neurosynaptic

networks for image recognition [41]. Recently, there has also been work on developing phase-change photonics using GST on Si waveguides [35,42,43]. Thus, both Si and SiN have been employed, although these two platforms have very distinct optical properties as well as relative advantages, both in the linear and nonlinear regimes. Given their different physical properties, especially thermal properties such as thermal conductivity and heat capacity, this would lead to different operational dynamics in the PCOM cells. Hence, it would be ideal to have both of these platforms for comparison, leading to a deeper understanding and more proper usage.

In this paper, we quantitatively explore the differences between PCOM cells on Si and SiN platforms and highlight the advantages and disadvantages of both platforms. Si has a clear advantage over SiN in terms of integration, speed, and device footprint due to the higher mode confinement. However, as we show, SiN has better energy efficiency because of its lower thermal conductivity. We particularly focus our experimentation (in terms of optical properties) on wavelengths in the C (1530–1565 nm) and L (1565–1625 nm) bands, as these are the most widely used bands for communications, although most of the analysis is more widely applicable. Our experimental results and analysis serve to provide a roadmap for this rapidly growing field.

2. RESULTS AND DISCUSSION

A. Material and Device Structure Comparison

Figure 1 compares the refractive indices [Fig. 1(a)] and extinction coefficients [Fig. 1(b) in log 10 scale] of Si, stoichiometric SiN (grown via low pressure chemical vapor deposition), and GST measured with ellipsometry with a wavelength range from 250 to 1690 nm. We focus on the telecommunications wavelength C and L bands (1530–1565 nm, 1565–1625 nm) where the optical contrast between the crystalline and amorphous states of GST is larger. It shows from Fig. 1(a) that the real part of refractive index of Si is significantly higher than that of SiN. This leads to stronger confinement of the optical mode within Si waveguides, causing a smaller and denser integration, but with higher sensitivity to sidewall roughness and geometric variations. Thus, tolerance analysis and calibration of fabrication processes for Si photonic devices are more crucial than for SiN devices.

Importantly, the contrast between Si and GST (both the amorphous and crystalline states) at telecommunication wavelengths is smaller compared with SiN. The similarity in refractive index between Si and amorphous GST on the one hand leads to lower scattering losses at the GST interface (see Fig. 3) and has been exploited to create tunable dielectric metasurfaces [44]; on the other hand, this causes weaker evanescent field coupling and thus smaller dynamic changes. From Fig. 1(b), imaginary parts of both Si and SiN are very low in the optical telecommunication bands, leading to propagation losses 0.1–0.5 dB/cm for Si and 0.04–1.37 dB/cm for SiN, respectively [45]. However, SiN waveguides have a much wider spectral range of transparency than that of Si, spanning from the visible to the infrared. Provided that the optical contrast between the amorphous and crystalline GST can be improved, this could enable phase-change photonics at visible wavelengths. In any case, a suitable substrate needs to be decided carefully, depending on the application and spectral regions of interest.

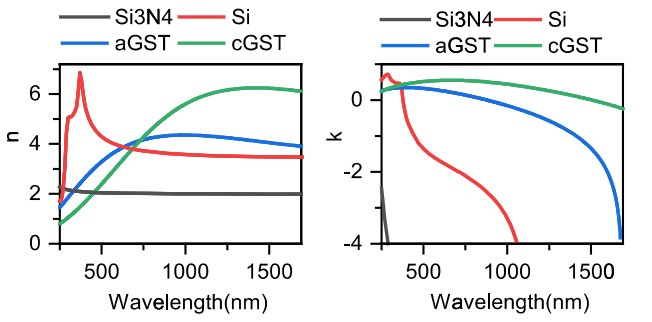

Fig. 1. Refractive indices of Si, Si_3N_4, and GST in their amorphous and crystalline states. (a) Real and (b) imaginary parts of refractive indices measured by ellipsometry.

Figures 2(a) and 2(b) illustrate the basic structure of an evanescently coupled PCOM cell based on an Si platform. Optical images of a completed computing cell are shown in Fig. 2(c), where GST has been sputtered on top of the waveguide. Light is coupled into the waveguide from optical fibers via grating couplers [shown in Fig. 2(c)]. For a single partially etched grating coupler, the coupling efficiency is about 40%. Figure 2(d) shows the transmission spectra of a bare Si waveguide (black curve), a Si cell with a 4-μm-long amorphous GST (red curve), and the same cell with crystalline GST, which was annealed on a hot plate at 250°C for 10 min (blue curve). After crystallization, the loss increases significantly due to absorption by the GST, which decreases the total transmission of the device. We see that amorphous GST has about 98% transmission, while the transmission reduces to about 25% in the crystalline state in a 4-μm-long device by measuring the transmission spectrum before GST deposition, and before and after crystallization.

Taking into account the refractive indices of GST, Si, and SiN, we simulated both mode profiles and light propagation in waveguides with a 10-nm-thick, 4-μm-long GST on top. Figures 3(a) and 3(b) show $|E|$ profiles at cross section. Figures 3(e) and 3(f) show propagation of the fundamental TE mode. As a comparison, the lower figures show SiN platform information accordingly, which has been commonly used in previous works [4,29,38,40]. The smaller contrast between the refractive indices of GST and Si leads to the lower reflection and scattering losses

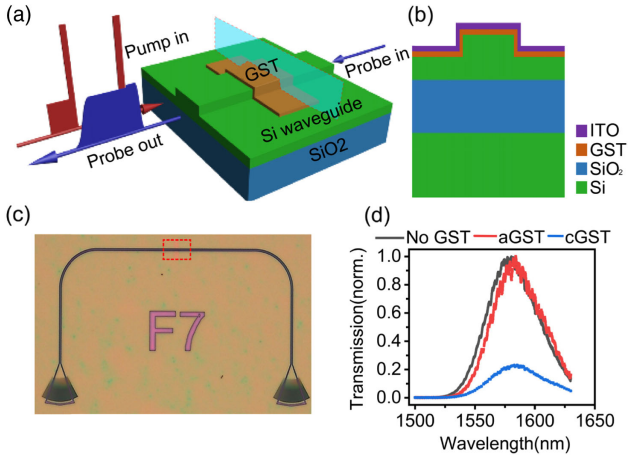

Fig. 2. Device design. (a) 3D overview and (b) cross-sectional view of an Si waveguide phase-change computing cell; (c) optical image of a GST photonic device. The material inside red dashed square is GST. (d) Normalized transmission spectrum of a typical photonic device without GST, with as-deposited amorphous GST, and with annealed crystalline GST.

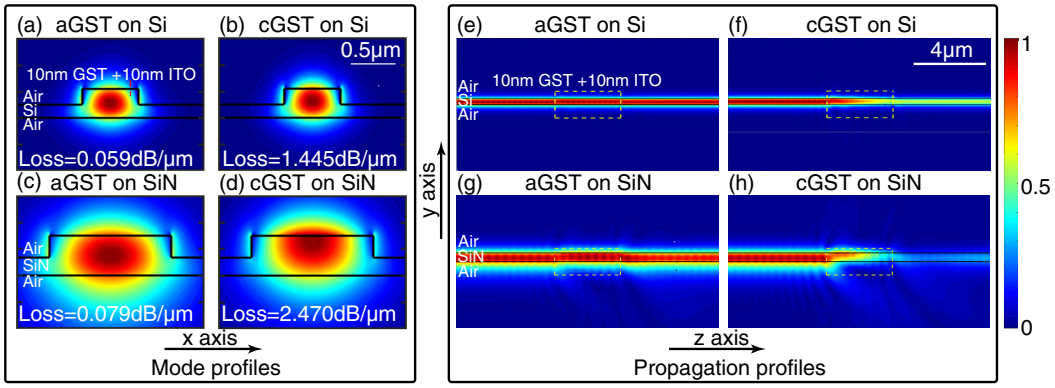

Fig. 3. Simulated eigenmode profiles and propagation profiles of the fundamental TE mode inside Si and SiN waveguides with GST. The 2D mode profile of Si waveguides with (a) amorphous and (b) crystalline GST and their SiN counterparts, (c) and (d). (e) and (f) show simulation results for propagation of the fundamental mode with 4 μm (e) amorphous and (f) crystalline GST on top of the waveguide. (g) and (h) are SiN waveguide comparisons.

observed compared with SiN, resulting in better matching between the optical mode in the bare waveguide and the phase-change material. Larger refractive index contrast between Si and air also leads to greater confinement of the fundamental TE mode, thus enabling a smaller waveguide width of 500 nm versus 1.3 μm for SiN. The reduction of evanescent coupling to the GST is a side effect of confining the optical mode to the core of the Si waveguide, leading to lower propagation loss in both states compared with SiN–GST waveguides.

The propagation loss can be calculated from the simulated complex effective refractive index,

$$\alpha = \frac{4\pi\,\mathrm{Im}(n_{\mathrm{eff}})}{\lambda}.$$

For a 4-μm-long device, we expect to see the transmission decrease from 95% in the amorphous state (0.059 dB/μm) to 26% in the crystalline state (1.445 dB/μm). This is in good agreement with our experimental results as shown in Fig. 2(d), in which the normalized transmission decreases from 96% to 23%. To achieve a certain on–off contrast, the PCOM cell on the Si platform requires a longer device length compared with SiN due to a lower propagation loss.

B. Dynamic Response during Amorphization

In this section, we compare the dynamic thermal and optical response of both platforms. Figure 4 shows the dynamic response of the amorphization process induced by a rectangular optical pulse with varied amplitude and pulse width. We first simulate the thermal response of crystalline GST to an optical pulse with increased amplitude and plot the temperature rise in the GST patch after a 20 ns rectangular pulse, with varied amplitude from 2 to 10 mW [solid and dashed lines indicate those for SiN and Si platforms, respectively, in Fig. 4(b)]. Figure 4(a) shows the spatial distribution of temperature in the device with 10 mW input pulse. The position of the maximum temperature is shown as a black dot [time-dependence of the temperature at this position is shown in Fig. 4(b)]. We observe that the temperature of the GST on the Si waveguide rises more quickly, but saturates to a lower peak temperature compared to SiN. We attribute this to two competing effects. First, since the volume of GST is smaller for the Si waveguide due to a smaller waveguide footprint, GST absorbs more energy; however, since the thermal conductivity of Si is much higher than that of SiN (thermal conductivity for bulk material data from [46,47]),

$$\kappa_{\mathrm{silicon}} = 148\ \mathrm{Wm}^{-1}\,\mathrm{K},$$

$$\kappa_{\mathrm{Si_3N_4}} = 43\ \mathrm{Wm}^{-1}\,\mathrm{K}.$$

Si waveguides experience quicker heat dissipation than SiN, thus saturating at a lower temperature for the same amount of optical power. Since Si loses a larger fraction of heat to the partially etched Si slab layer, we deduce that it can be more advantageous to use shorter pulses with higher amplitudes for phase-change devices on Si waveguides. This conclusion also agrees with experiments we did on devices [see Fig. 5(c)] for similar transmission changes; GST on Si requires about 3 times the amount of energy consumption as SiN.

In Figs. 4(c) and 4(d), we plotted the experimentally measured thermo-optic response of a Si phase-change device by sending a rectangular pulse for amorphization. Due to the strong thermo-optic effect in GST [48], the absorption is a function of device temperature, which produces a delay dead time in programming before reaching equilibrium. Here we got the dead time of the device t_{deadtime} as the time duration for transmitted power inside a waveguide to go from the lowest transmission point $T_{\mathrm{final\ state}}$ to a specific transmission point $\frac{1}{e}\cdot T_{\mathrm{final\ state}}$ from [4],

$$t_{\mathrm{deadtime}} = t_{\frac{1}{e}\cdot T_{\mathrm{final\ state}}} - t_{T_{\mathrm{final\ state}}}.$$

In data storage and in-memory computing, the dead time determines how quickly the state can be read after sending a programming pulse. We measured the dead time for Si phase-change cells and compared them with the SiN counterparts from [4]. Figure 4(e) shows that the dead time for devices with Si waveguides is nearly a quarter of that of SiN, thanks to the much higher thermal conductivity and smaller device footprint of Si. Thus, the higher thermal conductivity of Si allows faster write–read operations than SiN, considering a pulse width greater than 20 ns. Figure 4(f) is a zoomed-in comparison between two different pulse parameters on Si waveguides: varying amplitude with fixed duration (red) and varying time duration with fixed amplitude (blue). Increasing the pulse amplitude causes the dead time to increase, but increasing the pulses' duration does not, since GST reaches thermal equilibrium

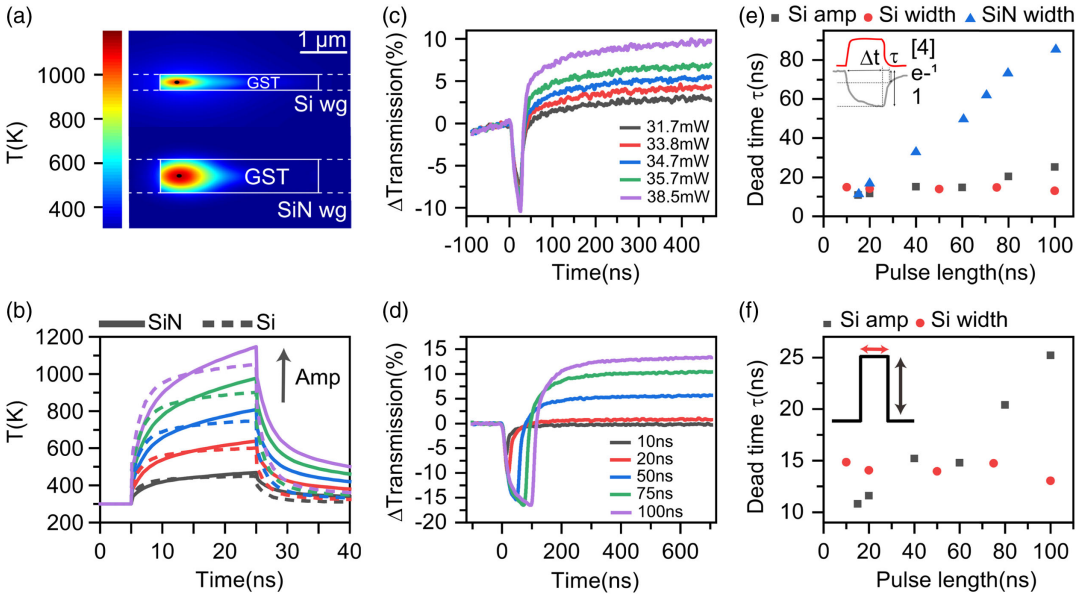

Fig. 4. Simulation and experimental results of dynamic response during amorphization process. (a) Temperature distribution maps from the top view for 4 μm GST on top of 500 nm Si waveguide and 1.3 μm SiN waveguide with 10 mW 20 ns pulse. A black dot is deposited on the position that has the highest temperature. (b) Simulated temperature changes for pump pulses with increasing amplitude. Fixed 20 ns rectangular pulses with power of 2, 4, 6, 8, 10 mW are sent to Si and SiN devices. (c)–(d) are thermo-optical changes taken with a high-speed photodetector with variation of (c) pump amplitude and (d) time width. (e) is dead time (definition from [4]) comparison between amplitude amorphization modulation and time width amorphization modulation methods, and with SiN devices from [4]. (f) is zoomed-in dead time comparison between these two modulation methods on Si waveguides.

and a similar device temperature with pulses greater than 10 ns, according to the simulations in Fig. 4(b). A constant dead time can be observed for pulses with a fixed amplitude and increased duration.

C. Switching Threshold and Energy Consumption

We now compare energy consumption. Figure 5 shows energy consumption and the switching threshold for achieving amorphization for Si and SiN waveguides with GSTs of different lengths. Figure 5(a) shows a heat map of energy consumption and a bar chart of transmission changes for an Si waveguide with 2-μm-long and 4-μm-long crystalline GST on top, respectively. The 4-μm device has a lower switching threshold so as to observe nonvolatile changes. The obtained switching contrast is proportional to the length of the GST from Fig. 5(b), in agreement with what is observed for the SiN platform [48]. Figure 5(c) illustrates that the higher thermal conductivity of Si waveguides causes greater energy consumption compared with that of SiN when an equivalent change in transmission is reached. Switching data of 5-μm GST on top of SiN waveguides from Ref. [48] are plotted in Fig. 5(c) as a comparison with results on Si (the closest device dimension in the literature). Yet more precise measurements need to be done in order to know the accurate energy consumption for ultrafast subnanosecond applications.

D. Demonstration of Single-Pulse Recrystallization on Si

As previously demonstrated on the SiN platform [25], it is also possible to achieve full recrystallization from any initial state using a single pulse on an Si platform. In Fig. 6(a), we show nonvolatile, multilevel operation of our devices with varied optical power of the amorphization pulse (25 ns duration). The amorphization power consumption for different levels is shown in Fig. 6(b).

The pulse power and change in transmission of the recrystallization process are shown in Figs. 6(c) and 6(d), respectively. Here we use double-step pulses with an initial short pulse with a high power (25 ns, 58.75 mW) followed by a long tail with a low power (23.5 mW with varied time width from 300 to 600 ns) to switch a 4-μm-long device on top of an Si waveguide. This allows us to quickly heat up the GST above the crystallization temperature until it reaches a partially or fully crystalline state. We observed that more energy is required to achieve a similar transmission contrast in Si compared to a previous demonstration in SiN [4], and we attribute this to the higher thermal conductivity of the Si waveguides and decreased evanescent coupling due to a stronger mode confinement. The power consumption can be reduced with a subnanosecond amorphization pulse, while the evanescent coupling can be enhanced through using resonant structures [49,50], or by simply reducing the waveguide thickness or width [40].

With the same pulse sequence, the device was programmed over many cycles. We plotted the final state of the device as a function of recrystallization time and the programming error, as shown in Fig. 6(e). We observed a maximum contrast of 12% for the 4-μm device, which is lower than for those devices on SiN [25] and agrees well with our results in Fig. 5(c). In the second step, with increased pulse width, we crystallized the GST to reach the fully crystalline state. Using the double-step pulse waveform simplifies pulse sequencing for multilevel operation in photonic computing. Pulses with decreased energy were used to incrementally recrystallize the GST until the desired level was reached. For switching from the maximum transmission (i.e., amorphous) to the minimum transmission (i.e., crystalline), 19 pulses with energies ranging from 370 to 600 pJ were required with a total

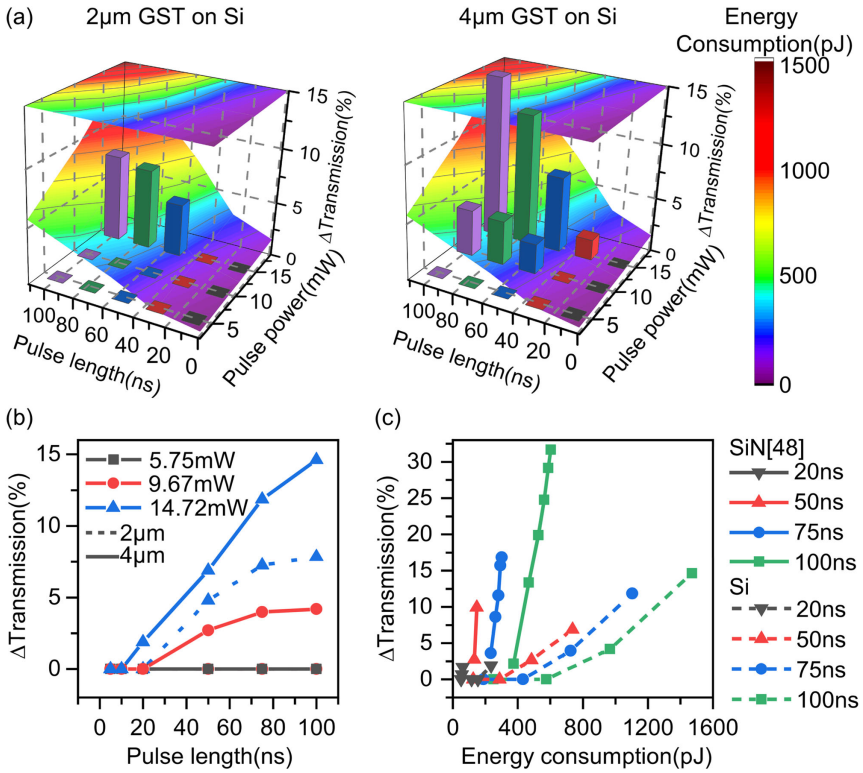

Fig. 5. Relationship among switching parameters, optical transmitted signal, and energy consumption. Photonic computing unit with 2 μm (length along transmission) functional PCOM and 4 μm functional PCOM are shown with solid line and dashed line separately. (a) shows 3D maps for energy needed and associated transmission changes for 2 and 4 μm devices separately. (b) Relative transmission changes with the increase of time width of pump pulses from 5 to 100 ns as a comparison between 2 and 4 μm devices. (c) Comparison of energy consumption of Si and SiN devices. The length of GST is 4 μm on Si and 5 μm on the SiN device from [48], with pulse widths from 20 to 100 ns. Every data point is averaged from 300 repeated measurements.

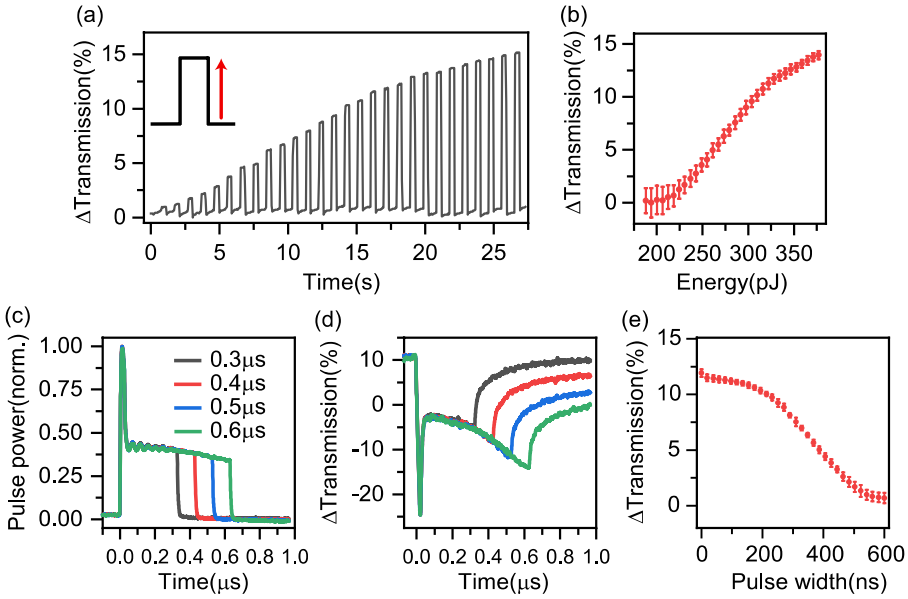

Fig. 6. Single-pulse recrystallization on Si waveguides. (a) Independent multilevel states with pulse amplitude modulation; (b) programming power for different levels in (a) accordingly; (c) experimental crystallization pulses and (d) device corresponding response signal with double-step crystallization pulses with 25 ns for the first pulse and 300–600 ns for the second pulse time width variation; (e) error bar of relative transmission contrast recrystallization second step time width modulation.

Table 1. Silicon versus SiN Integrated Photonic Devices Performance Comparison[a]

Waveguide Type	Si	SiN
Refractive index at 1550 nm	$3.478 + 0i$	$1.9894 + 0i$
Refractive index at 470 nm	$4.491 + 0.76i$	$2.049 + 0i$
Effective refractive index with 10 nm crystalline GST on top	$2.705 + 0.04i$	$1.675 + 0.07i$
Thermal conductivity ($W \cdot m^{-1}K^{-1}$)	148	43
Footprint of the GST cell (functional part: thickness × length × lateral size) (μm^3)	$0.01 \times 4 \times 0.45$	$0.01 \times 4 \times 1.3$
Propagation loss (GST amorphous) (dB/μm)	0.059	0.079
Propagation loss (GST crystalline) (dB/μm)	1.445	2.470
Switching dead time with 10 ns pump pulse (ns)	10	10
Switching dead time with 100 ns pump pulse (ns)	13	87
Smallest nonvolatile amorphization energy (pJ)	388.4	42 [4]

[a]Experimental results are using data of 4 μm devices.

programming energy of 9.5 nJ and duration of 3.8 μs. Similar approaches have also been demonstrated with picosecond and femtosecond pulses [38,51,52] but require multiple recrystallization pulses of decreasing amplitude to reach the desired intermediate state. Here, we demonstrated multilevel operation using a single pulse with pulse width ranging from 25 to 625 ns to achieve 30 distinct transmission levels without knowledge of the prior state.

3. CONCLUSION

Table 1 shows the summary of our experimental evaluation of the key trade-offs between an Si platform and an SiN platform. Differences in substrates and parameters (refractive indices and thermal conductivity) cause changes to device footprints and optical properties. An Si platform allows a more compact footprint and the reduction of time in amorphization compared with an SiN platform. The energy consumption is, however, higher for enhancing transmission contrast due to the fast energy dissipation from the Si slab. This disadvantage may be overcome by using strip waveguides rather than rib waveguides. Thus, SiN is preferred for applications in the visible and near-infrared spectral regions, whereas an Si platform with compact footprints is preferred for telecommunications data processing and in-memory computing [39] with large scalability in matrix operation.

For computing applications, Si platforms have key advantages, such as (a) large-scale support from existing CMOS foundry capabilities and compatibility of integration with other on-chip active electronic and photonic components so as to build up an entire optoelectronic computing system; (b) high data-processing speed and superior heat transport; (c) compact footprint; and (d) low-loss light propagation in telecommunications wavelength bands. Recently, the combination of Si and SiN waveguides has also been explored [53], which may be a good way to make use of the advantages of both platforms in the future.

In conclusion, we report key differences between these two important platforms in terms of operational speed, footprint, and energy consumption. We characterize the reliability of single-pulse modulation on an Si platform and give a comparison with state-of-the-art programming techniques. Due to the higher mode confinement and thermal conductivity, Si has a clear advantage over SiN in terms of integration, speed, and device footprint. However, all-optical switching is more efficient in SiN platforms, which may thus be preferred in conditions where integrated electronics and photonics are not required on the same chip.

APPENDIX A: DESIGN AND FABRICATION

To fabricate the waveguides, we used an SOI substrate with a 220 nm device layer and 3 μm buried oxide. Our device is illustrated in Fig. 2, where the phase-change material (GST) is evanescently coupled to the optical mode of the Si waveguide, enabling all-optical WRITE, READ, and ERASE operations. Electron beam lithography is used to pattern the device, and dry etching is used to partially etch down Si waveguides (120 nm etching depth). Subsequently, a 10 nm functional layer of GST and a 10 nm protective layer of indium–tin–oxide (ITO) are deposited on the top of the waveguide using RF sputtering (30 W RF power, 5 mTorr Ar atmosphere, and 2×10^{-6} Torr base pressure).

APPENDIX B: MEASUREMENT SET-UP

We use a 1590 nm laser source, amplified with an L-band erbium-doped fiber amplifier (EDFA) to optically switch the state of the GST and a 1610 nm continuous probe laser to monitor the transmission of light. To shape the optical pulses, an arbitrary function generator (Tektronics 100 MHz AFG3102C) is used to send RF pulses to a high-speed electro-optic modulator (EOM). The nonlinear response of the EOM is compensated for by the shape of the input RF pulse such that the pulse shape we describe above reflects the shape of the optical pulse after the EDFA rather than the input electrical pulse. Optical bandpass filters are used in both beam paths to reduce the influence of parasitic wavelengths. At the end of both paths, we use low-noise-sensitive photodetectors to record the dynamic change of the transmission of the light and a fast-speed sampling oscilloscope to record the thermo-optical effect of the device when it is excited by writing pulses. With this measurement scheme, we are able to observe phase transitions in real time with subnanosecond resolution. In order to control the power of the pulses sent to the device, we use a tunable optical attenuator to control the power of the pump seed laser before the EOM. In order to reduce the fluctuation of the polarization of the probe seed laser, we also added an in-line fiber polarizer, a polarization controller, and reference photodiode between the probe laser and device to remove the noise from polarization drift due to thermal fluctuations in the setup.

Funding. Engineering and Physical Sciences Research Council (EP/J018694/1, EP/M015130/1, EP/M015173/1); Deutsche Forschungsgemeinschaft (PE1832/2-1); Horizon 2020 Framework Programme (780848).

Acknowledgment. All authors thank the collaborative nature of European science for allowing this work to be carried out. This research was supported via the Engineering and Physical Sciences Research Council Manufacturing, the Wearable and Flexible Technologies (WAFT) collaboration, and the Chalcogenide Advanced Manufacturing Partnership. We thank Dr. Carlos Rios for discussion about theoretical analysis.

Disclosures. The authors declare no conflicts of interest.

REFERENCES

1. G. E. Moore, "Cramming more components onto integrated circuits," Electronics **38**, 114–117 (1965).
2. M. P. Frank, "The physical limits of computing," Comput. Sci. Eng. **4**, 16–26 (2002).
3. I. L. Markov, "Limits on fundamental limits to computation," Nature **512**, 147–154 (2014).
4. C. Rios, M. Stegmaier, P. Hosseini, D. Wang, T. Scherer, C. D. Wright, H. Bhaskaran, and W. H. P. Pernice, "Integrated all-photonic non-volatile multi-level memory," Nat. Photonics **9**, 725–732 (2015).
5. A. Klein, G. Masri, H. Duadi, K. Sulimany, O. Lib, H. Steinberg, S. A. Kolpakov, and M. Fridman, "Ultrafast rogue wave patterns in fiber lasers," Optica **5**, 774–778 (2018).
6. C. Wang, M. Zhang, X. Chen, M. Bertrand, A. Shams-Ansari, S. Chandrasekhar, P. Winzer, and M. Lončar, "Integrated lithium niobate electro-optic modulators operating at CMOS-compatible voltages," Nature **562**, 101–104 (2018).
7. T. J. Seok, K. Kwon, J. Henriksson, J. Luo, and M. C. Wu, "Wafer-scale silicon photonic switches beyond die size limit," Optica **6**, 490–494 (2019).
8. E. S. Magden, N. Li, M. Raval, C. V. Poulton, A. Ruocco, N. Singh, D. Vermeulen, E. P. Ippen, L. A. Kolodziejski, and M. R. Watts, "Transmissive silicon photonic dichroic filters with spectrally selective waveguides," Nat. Commun. **9**, 3009 (2018).
9. P. J. Winzer, D. T. Neilson, and A. R. Chraplyvy, "Fiber-optic transmission and networking: the previous 20 and the next 20 years [Invited]," Opt. Express **26**, 24190–24239 (2018).
10. H. Xiao, Z. Liu, X. U. Han, J. Yang, G. Ren, A. Mitchell, and Y. Tian, "On-chip reconfigurable and scalable optical mode multiplexer/demultiplexer based on three-waveguide-coupling structure," Optics Express **26**, 22366–22377 (2018).
11. M. Feng, J. Wang, R. Zhou, Q. Sun, H. Gao, Y. Zhou, J. Liu, Y. Huang, S. Zhang, M. Ikeda, H. Wang, Y. Zhang, Y. Wang, and H. Yang, "On-chip integration of GaN-based laser, modulator, and photodetector grown on Si," IEEE J. Sel. Top. Quantum Electron. **24**, 8200305 (2018).
12. Y. Salamin, P. Ma, B. Baeuerle, A. Emboras, Y. Fedoryshyn, W. Heni, B. Cheng, A. Josten, and J. Leuthold, "100 GHz plasmonic photodetector," ACS Photon. **5**, 3291–3297 (2018).
13. C. Ye, K. Liu, R. A. Soref, and V. J. Sorger, "A compact plasmonic MOS-based 2×2 electro-optic switch," Nanophotonics **4**, 261–268 (2015).
14. B. W. Jia, K. H. Tan, W. K. Loke, S. Wicaksono, and S. F. Yoon, "Integration of an InSb photodetector on Si via heteroepitaxy for the mid-infrared wavelength region," Opt. Express **26**, 7227–7234 (2018).
15. B. Zheng, H. Zhao, B. Cerjan, S. Yazdi, E. Ringe, P. Nordlander, and N. J. Halas, "A room-temperature mid-infrared photodetector for on-chip molecular vibrational spectroscopy," Appl. Phys. Lett. **113**, 101105 (2018).
16. R. Soref, "Silicon photonics: a review of recent literature," Silicon **2**, 1–6 (2010).
17. M. Paniccia, "Integrating silicon photonics," Nat. Photonics **4**, 498–499 (2010).
18. L. Chrostowski, H. Shoman, M. Hammood, H. Yun, J. Jhoja, E. Luan, S. Lin, A. Mistry, D. Witt, N. A. F. Jaeger, S. Shekhar, H. Jayatilleka, P. Jean, S. Belanger-de Villers, J. Cauchon, W. Shi, C. Horvath, J. Bachman, K. Setzer, M. Aktary, S. Patrick, R. Bojko, X. Wang, T. F. de Lima, A. Tait, P. Prucnal, D. Hagan, D. Stevanovic, and A. Knights, "Silicon photonic circuit design using rapid prototyping foundry process design kits," IEEE J. Sel. Top. Quantum Electron. **25**, 8201326 (2019).
19. H. Zhang, L. Zhou, J. Xu, N. Wang, H. Hu, L. Lu, B. M. A. Rahman, and J. Chen, "Nonvolatile waveguide transmission tuning with electrically-driven ultra-small GST phase-change material," Sci. Bull. **64**(11), 782–789 (2019).
20. A. N. Tait, T. F. de Lima, M. A. Nahmias, H. B. Miller, H.-T. Peng, B. J. Shastri, and P. R. Prucnal, "Silicon photonic modulator neuron," Phys. Rev. Appl. **11**, 064043 (2019).
21. K. Wu, C. Guo, H. Wang, X. Zhang, J. Wang, and J. Chen, "All-optical phase shifter and switch near 1550nm using tungsten disulfide (WS_2) deposited tapered fiber," Opt. Express **25**, 17639–17649 (2017).
22. Y. Li, W. Chen, T. Dai, and P. Wang, "Nonvolatile integrated optical phase shifter with flash memory technology," Appl. Phys. Express **12**, 102005 (2019).
23. M. Rudé, J. Pello, R. E. Simpson, J. Osmond, and G. Roelkens, "Optical switching at 1.55 μm in silicon racetrack resonators using phase change materials," Appl. Phys. Lett. **103**, 141119 (2013).
24. N. Youngblood, C. Ríos, E. Gemo, J. Feldmann, Z. Cheng, A. Baldycheva, W. H. Pernice, C. D. Wright, and H. Bhaskaran, "Tunable volatility of $Ge_2Sb_2Te_5$ in integrated photonics," Adv. Funct. Mater. **29**, 1807571 (2019).
25. X. Li, N. Youngblood, C. Ríos, Z. Cheng, C. D. Wright, W. H. Pernice, and H. Bhaskaran, "Fast and reliable storage using a 5 bit, nonvolatile photonic memory cell," Optica **6**, 1–6 (2019).
26. C. R. de Galarreta, I. Sinev, A. M. Alexeev, P. Trofimov, K. Ladutenko, S. G.-C. Carrillo, E. Gemo, A. Baldycheva, V. K. Nagareddy, J. Bertolotti, and C. D. Wright, "All-dielectric silicon/phase-change optical metasurfaces with independent and reconfigurable control of resonant modes," arXiv:1901.04955 (2019).
27. G. Rodriguez-Hernandez, P. Hosseini, C. Ríos, C. D. Wright, and H. Bhaskaran, "Mixed-mode electro-optical operation of $Ge_2Sb_2Te_5$ nanoscale crossbar devices," Adv. Electron. Mater. **3**, 1700079 (2017).
28. S. Wen, Y. Meng, M. Jiang, and Y. Wang, "Multi-level coding-recoding by ultrafast phase transition on $Ge_2Sb_2Te_5$ thin films," Sci. Rep. **8**, 4979 (2018).
29. J. Von Keitz, J. Feldmann, N. Gruhler, C. Ríos, D. Wright, H. Bhaskaran, and W. H. P. Pernice, "Reconfigurable nanophotonic cavities with non-volatile response," ACS Photon. **5**, 4644–4649 (2018).
30. K. Nozaki, A. Shinya, S. Matsuo, Y. Suzaki, T. Segawa, T. Sato, Y. Kawaguchi, R. Takahashi, and M. Notomi, "Ultralow-power all-optical RAM based on nanocavities," Nat. Photonics **6**, 248–252 (2012).
31. Z. Cheng, C. Ríos, N. Youngblood, C. D. Wright, W. H. P. Pernice, and H. Bhaskaran, "Device-level photonic memories and logic applications using phase-change materials," Adv. Mater. **30**, 1802435 (2018).
32. J. Wang, S. Paesani, Y. Ding, R. Santagati, P. Skrzypczyk, A. Salavrakos, J. Tura, R. Augusiak, L. Mančinska, D. Bacco, D. Bonneau, J. W. Silverstone, Q. Gong, A. Acín, K. Rottwitt, L. K. Oxenløwe, J. L. O'Brien, A. Laing, and M. G. Thompson, "Multidimensional quantum entanglement with large-scale integrated optics," Science **360**, 285–291 (2018).
33. Z. Lu, H. Yun, Y. Wang, Z. Chen, F. Zhang, N. A. F. Jaeger, and L. Chrostowski, "Broadband silicon photonic directional coupler using asymmetric-waveguide based phase control," Opt. Express **23**, 3795–3808 (2015).
34. A. V. Kolobov, P. Fons, J. Tominaga, and S. R. Ovshinsky, "Vacancy-mediated three-center four-electron bonds in GeTe-Sb_2Te_3 phase-change memory alloys," Phys. Rev. B **87**, 165206 (2013).
35. J. Zheng, A. Khanolkar, P. Xu, S. Colburn, S. Deshmukh, J. Myers, J. Frantz, E. Pop, J. Hendrickson, J. Doylend, N. Boechler, and A. Majumdar, "Non-volatile quasi-continuously programmable silicon photonics using phase-change materials (conference presentation)," Proc. SPIE **10923**, 109230U (2019).
36. J. Zheng, A. Khanolkar, P. Xu, S. Colburn, S. Deshmukh, J. Myers, J. Frantz, E. Pop, J. Hendrickson, J. Doylend, N. Boechler, and A. Majumdar, "GST-on-silicon hybrid nanophotonic integrated circuits: a non-volatile quasi-continuously reprogrammable platform," Opt. Mater. Express **8**, 1551–1561 (2018).
37. P. Xu, J. Zheng, J. K. Doylend, and A. Majumdar, "Low-loss and broadband nonvolatile phase-change directional coupler switches," ACS Photon. **6**, 553–557 (2019).
38. J. Feldmann, M. Stegmaier, N. Gruhler, C. Riós, H. Bhaskaran, C. D. Wright, and W. H. P. Pernice, "Calculating with light using a chip-scale all-optical abacus," Nat. Commun. **8**, 1–8 (2017).

39. C. Ríos, N. Youngblood, Z. Cheng, M. Le Gallo, W. H. P. Pernice, C. D. Wright, A. Sebastian, and H. Bhaskaran, "In-memory computing on a photonic platform," Sci. Adv. **5**, eaau5759 (2019).
40. Z. Cheng, C. Ríos, W. H. P. Pernice, C. D. Wright, and H. Bhaskaran, "On-chip photonic synapse," Sci. Adv. **3**, 1–7 (2017).
41. J. Feldmann, N. Youngblood, C. D. Wright, H. Bhaskaran, and W. H. P. Pernice, "All-optical spiking neurosynaptic networks with self-learning capabilities," Nature **569**, 208–214 (2019).
42. E. Yalon, I. M. Datye, J. S. Moon, K. A. Son, K. Lee, and E. Pop, "Energy-efficient indirectly heated phase change RF switch," IEEE Electron Device Lett. **40**, 455–458 (2019).
43. H. Zhang, L. Zhou, L. Lu, J. Xu, N. Wang, H. Hu, B. M. A. Rahman, Z. Zhou, and J. Chen, "Miniature multilevel optical memristive switch using phase change material," ACS Photon. **6**, 2205–2212 (2019).
44. A. Alexeev, C. R. de Galarreta, S. G.-C. Carrillo, I. S. Sinev, A. K. Samusev, E. Gemo, V. K. Nagareddy, Y.-Y. Au, and C. D. Wright, "Tunable dielectric metadevices enabled by phase-change materials," in *European Phase Change and Ovonic Symposium* (2017).
45. P. Muñoz, G. Micó, L. A. Bru, D. Pastor, D. Pérez, J. D. Doménech, J. Fernández, R. Baños, B. Gargallo, R. Alemany, A. M. Sánchez, J. M. Cirera, R. Mas, and C. Domínguez, "Silicon nitride photonic integration platforms for visible, near-infrared and mid-infrared applications," Sensors **17**, 2088 (2017).
46. "Thermal conductivity: silicon," https://www.efunda.com/materials/elements/TC_Table.cfm?Element_ID=Si.
47. "Silicon nitride (Si3N4) properties and applications," https://www.azom.com/properties.aspx?ArticleID=53.
48. C. Rios, M. Stegmaier, Z. Cheng, N. Youngblood, C. D. Wright, W. H. P. Pernice, and H. Bhaskaran, "Controlled switching of phase-change materials by evanescent-field coupling in integrated photonics [Invited]," Opt. Mater. Express **8**, 2455–2470 (2018).
49. N. Farmakidis, N. Youngblood, X. Li, J. Tan, J. L. Swett, Z. Cheng, C. D. Wright, W. H. P. Pernice, and H. Bhaskaran, "Plasmonic nanogap enhanced phase-change devices with dual electrical-optical functionality," Sci. Adv. **5**, eaaw2687 (2019).
50. M. Rudé, R. E. Simpson, R. Quidant, V. Pruneri, and J. Renger, "Active control of surface plasmon waveguides with a phase change material," ACS Photon. **2**, 669–674 (2015).
51. Y. Liu, M. M. Aziz, A. Shalini, C. D. Wright, and R. J. Hicken, "Crystallization of $Ge_2Sb_2Te_5$ films by amplified femtosecond optical pulses," J. Appl. Phys. **112**, 123526 (2012).
52. M. Stegmaier, C. Ríos, H. Bhaskaran, C. D. Wright, and W. H. P. Pernice, "Nonvolatile all-optical 1×2 switch for chipscale photonic networks," Adv. Opt. Mater. **5**, 1600346 (2017).
53. Q. Wilmart, H. El Dirani, N. Tyler, D. Fowler, S. Malhouitre, S. Garcia, M. Casale, S. Kerdiles, K. Hassan, C. Monat, X. Letartre, A. Kamel, M. Pu, K. Yvind, L. Oxenløwe, W. Rabaud, C. Sciancalepore, B. Szelag, and S. Olivier, "A versatile silicon-silicon nitride photonics platform for enhanced functionalities and applications," Appl. Sci. **9**, 255 (2019).